IEEE Photonics Journal
An IEEE Photonics Society Publication

Retinal Laser Lesion Visibility in Simultaneous Ultra-High Axial Resolution Optical Coherence Tomography

Volume 6, Number 6, December 2014

Patrick Steiner
Volker Enzmann
Christoph Meier
Boris Považay
Jens H. Kowal

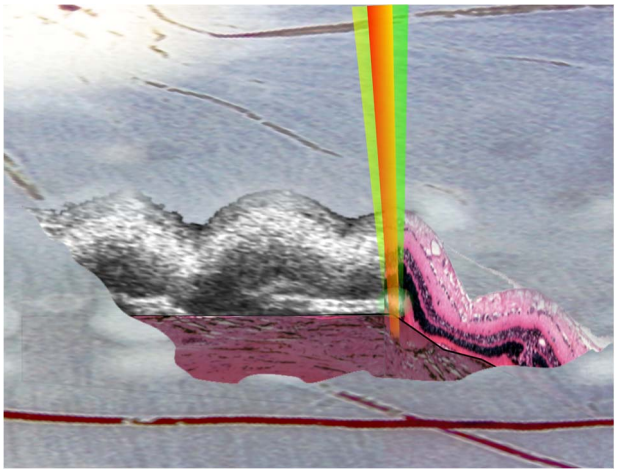

DOI: 10.1109/JPHOT.2014.2374594
1943-0655 © 2014 IEEE

Retinal Laser Lesion Visibility in Simultaneous Ultra-High Axial Resolution Optical Coherence Tomography

Patrick Steiner,[1,2] Volker Enzmann,[3] Christoph Meier,[2] Boris Považay,[2] and Jens H. Kowal[1,3]

[1]ARTORG Center, University of Bern, 3010 Bern, Switzerland
[2]HuCE OptoLab, Berne University of Applied Sciences, 2502 Biel, Switzerland
[3]Department of Ophthalmology, Inselspital, 3010 Bern, Switzerland

DOI: 10.1109/JPHOT.2014.2374594

Manuscript received October 9, 2014; revised November 14, 2014; accepted November 16, 2014. Date of current version December 8, 2014. Corresponding author: P. Steiner (e-mail: patrick.steiner@artorg.unibe.ch).

Abstract: *Ex vivo* porcine retina laser lesions applied with varying laser power (20 mW–2 W, 10 ms pulse, 196 lesions) are manually evaluated by microscopic and optical coherence tomography (OCT) visibility, as well as in histological sections immediately after the deposition of the laser energy. An optical coherence tomography system with 1.78 μm axial resolution specifically developed to image thin retinal layers simultaneously to laser therapy is presented, and visibility thresholds of the laser lesions in OCT data and fundus imaging are compared. Optical coherence tomography scans are compared with histological sections to estimate the resolving power for small optical changes in the retinal layers, and real-time time-lapse scans during laser application are shown and analyzed quantitatively. Ultrahigh-resolution OCT inspection features a lesion visibility threshold 40–50 mW (17% reduction) lower than for visual inspection. With the new measurement system, 42% of the lesions that were invisible using state-of-the-art ophthalmoscopic methods could be detected.

Index Terms: Retinal laser therapy, photocoagulation, optical coherence tomography, histology.

1. Introduction

Over the past few decades, retinal laser photocoagulation has been established as a successful treatment for a variety of retinal diseases such as age-related macula degeneration or diabetic retinopathy. However, laser photocoagulation shows the potential drawback of local overexposure that physically destroys different retinal layers. If not monitored, the thermal diffusion can seriously harm or irreversibly destroy neuronal layers as well as complete nerve trajectories [1]. Current assessment of the retinal lesions often relies on visual inspection using direct ophthalmoscopy or fluorescence imaging which is time-consuming and only offers limited interpretation of the laser damage. Ophthalmoscopically, the lesions only become visible as grayish spots after the coagulation of superficial tissue. Thus, an ophthalmoscopic assessment of the laser coagulation effects in deeper retinal layers is not possible. Recent studies by Koinzer *et al.* [2] have shown that ophthalmoscopic analysis of laser coagulation burns may be misleading regarding effective laser lesion size and total affected tissue area.

To overcome current limitations in assessing retinal laser lesions, optical coherence tomography (OCT) [3] is a promising modality to image the retina after laser treatment as it provides a volumetric representation of the optical properties of retinal tissue such as reflectivity or the distortion of retinal layers [4]. In their recent study, Koinzer *at al.* [2] reported first detectable changes 2h after treatment with an increased scattering to be located in the neuronal retina. However, when applying lasers for retinal treatment, the melanin in the RPE acts as the main absorber of commonly used treatment lasers emitting in the green and yellow spectral range [5], [6]. Thus, when imaging during or immediately after laser treatment it appears reasonable to expect the first biological, structural and successive optical changes to be localized in and around the retinal pigment epithelium (RPE). Various studies support the hypothesis that a considerable number of retinal diseases can be directly associated with pathological changes in, or degradation of the RPE monolayer [7]–[9]. Thus, the RPE as an important and extremely active biological interface and border between the choroid and the photoreceptor layer also constitutes the main target for laser photocoagulation.

Various experiments have been published discussing OCT imaging of laser lesions [10]–[13] including polarization sensitive OCT [14] and a proposed lesion classifier [15], however, to our best knowledge, to this date no data are available for OCT imaging with an axial resolution adapted for imaging thin retinal layers during or immediately after laser treatment. To detect laser induced alterations within the RPE/Bruch's complex, it may be sufficient to only detect a relatively abstract change in the OCT signal which contains the combined information of the signal carrying speckle and the direct structural information from the backscattered light. Since the speckle size is related to the resolution of the imaging system, a higher axial resolution will reveal additional information about the scattering structure of the retinal layers [16]. As a consequence, OCT systems for laser lesion monitoring should feature an axial resolution that facilitates imaging structural and optical changes in the RPE and adjacent layers. With the RPE monolayer being only 10–14 μm thick around the macula [17], [18], this leads to a required axial resolution of a few micrometers. Commercially available and clinical systems are typically limited to an axial resolution of around 6 μm as for most applications in ophthalmology a higher axial resolution is not a prerequisite and high axial resolution leads to higher technical complexity and costs of the OCT systems due to the $\lambda_c^2/\Delta\lambda$ relation of bandwidth and resolution.

In this paper, OCT volume scans of porcine eyes irradiated ex vivo with variable laser energies are recorded with a custom-made OCT system with 1.78 μm axial resolution. OCT volume scans and simultaneously acquired time-resolved point scans (Mscans) are presented and evaluated toward the visibility of the tissue changes with a focus on changes in the RPE and adjacent layers. OCT scans are compared to histological sections of the samples representing an overview of the tissue changes. The acquired data were evaluated strictly against the visibility of the lesions (OCT-fundus imaging) and the resolving power of the OCT system (OCT-histology). The histological sections were used solely to correlate OCT signal changes with tissue alterations after laser application. Interpretation of biological effects or the quantitative extent of laser damage was prevented by artifacts in the enucleated retinal tissue.

2. Optical Coherence Tomography System

The OCT system employed in this study was specifically designed to feature an axial resolution in the range of few micrometers in order to facilitate imaging of the small structures of the RPE layer while providing an A-Scan rate suitable for in-vivo measurements.

Because of the $\lambda_c^2/\Delta\lambda$ dependence of the axial resolution, a system with center wavelength $\lambda_c = 830$ nm was realized using a broadband superluminescent light-emitting diode (SLED) light source combining four SLED modules (EBS8C10, Exalos AG, Switzerland), resulting in a 3 dB bandwidth of $\Delta\lambda = 170$ nm and an axial resolution of 1.78 μm in air, which was determined by the intensity-based full width half maximum of the absolute value of the light source Fourier transform. The in-house developed spectrometer consists of a volume phase holographic dispersion grating with 1200 lp/mm, an optical system using spherical 2-inch optics, a custom made field flattening

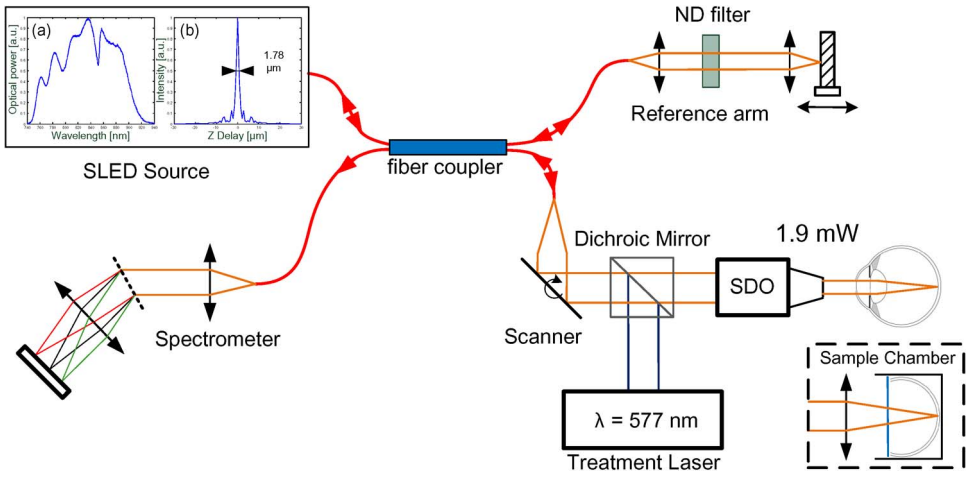

Fig. 1. Schematic setup of the FD-OCT system at 830 nm coupled to the laser photocoagulation therapy setup. The OCT setup includes light source, fiber coupler, dichroic mirror, and spectrometer, and the therapy system includes the treatment laser source and the scanning digital ophthalmoscope (SDO). OCT light source spectrum and PSF are shown in the insets on the top left. The box on the bottom right shows the alternative optical setup used if anterior segments were removed.

lens, and a 2048-pixel line scan camera (AVIIVA EM4, e2v, U.K.) with 70 kHz line rate. The OCT system was combined with the laser treatment system using a dichroic mirror as shown in Fig. 1.

The sample beam was focused onto the samples using a standard 2D galvo scanner unit and a SDO (Wild MedTec, Wien, Austria) with a retinal spot size of approximately 35 μm for in-vivo and time-resolved measurements. For measurements on porcine eyes with removed anterior segments, an achromatic focusing lens with f = 33 mm (retinal spot size approx. 13 μm) was employed. Spot sizes were measured and confirmed using a beam profiler (WinCamD-UHR, DataRay Inc., Bella Vista, CA, USA). For the experiments in this paper, the incident power of the OCT probing beam at the sample arm was set to 1.9 mW and reference arm power was adjusted using a simple neutral density damping element. Integration time of the OCT scans was set to a minimum value of 14 μs to achieve the highest frame rate. The sample focus position was controlled and optimized for each recording by simultaneously moving the delivery optics and the reference arm until signal quality and SNR reached a maximum. OCT volume data were recorded with two dimensional telecentric line scanning using the scanning unit.

To correct the large dispersion mismatch of the OCT system caused by the multiple lenses in the sample arm and intensified by the broad bandwidth of the light source, dispersion compensation glass (26 mm N-BK7) was added to the reference arm. Residual and higher order dispersion was compensated for numerically during post-processing of the OCT data. With the described system, a maximum sensitivity of 102 dB with an integration time of 14 μs was achieved with a fall-off of approximately 5 dB over the first mm and approximately 25 dB over the measurement range of 2.3 mm.

OCT data acquisition and post-processing was implemented in a proprietary LabVIEW framework (NI, Austin, Texas, USA). Averaging of OCT scans was enabled by the software but resulted in a reduced acquisition speed. Averaging was thus limited to a value of four consecutive scans without using frame-to-frame registration because of the static setup. Processed data were stretched and re-sampled frame by frame to correct for the difference in lateral and axial resolution.

3. Material and Methods

3.1. Sample Preparation

Porcine eyes were collected from a local slaughterhouse where sacrificing of the animal took place 1–4 hours before the experiments. Upon collection, the porcine eyes were stored on ice

and covered in DMEM solution (Gibco Life Technologies, Carlsbad, CA, USA) to prevent rapid degradation. Before exposure to the laser energy, the anterior segment including cornea and lens was carefully removed by circumbulbar cutting the eyes posterior to the limbus to prevent opacity effects of the cornea to have influence on the experiments. The vitreous was kept in place and covered with a round d = 20 mm microscope cover slip. The porcine eyes were fixated in a specifically designed sample chamber and subsequently treated with the treatment laser.

3.2. Treatment Laser

For the laser treatment, a prototype laser emitting at 577 nm (Merilas, Meridian AG, Thun, Switzerland) was used. The laser was operated in a quasi-continuous mode with pulse repetition frequency selectable between 15 kHz and 50 kHz, which, in all cases, exceeded the value for pulse effects in the tissue [19], [20]. Therefore, treatment effects and temperature distributions are similar or identical to cw irradiation. Threshold energy considerations in this paper are thus referenced to published values of cw (single pulse) laser coagulation.

The treatment laser was coupled into the setup using a standard 50 μm fiber with NA = 0.22 and guided onto the retina using a f = 35 mm achromatic collimating lens, a dichroic mirror and a fixed protected silver mirror. The collimated treatment laser was directly focused onto the porcine retina using a f = 120 mm focus lens. The optical setup featured a treatment laser spot size of approximately 130 μm on the retina. The retinal spot size was confirmed by microscopic inspection of the lesions. Lesions were placed using the stage of the SDO and the video feedback provided by the SDO camera chip. The laser lesions were set with trains of pulses adding up to a total irradiation time of 10 ms. Total applied energies varied from 0.7 to 20 mJ, which is equivalent to laser powers of between 70 mW and 2 W.

3.3. Histology

In this study, histological sections of the laser lesions were prepared to compare the structural changes to the alterations of optical properties detected with OCT as histology can be used to directly asses tissue damage caused by laser irradiation [21], [22].

After laser treatment, the enucleated porcine eyes were fixated in Davidson's solution mixed according to [23] for 24 h before the samples were washed in a flush mixture (60% ethanol, 40% tap water). The samples were then trimmed to an approximate size of 20 mm $\times$ 10 mm using high energy marker lesions as a reference and prepared for embedding by paraffinization. Samples were embedded in paraffin and cut using a microtome. Sections were taken every 30 μm and stained with H&E staining. Histological section were imaged with a transmitted-light microscope (AxioPlan 2, Carl Zeiss AG, Germany) with 20$\times$ magnification. For the purpose of matching the histological images with the OCT data, full tile scan images (2.5 mm $\times$ 15 mm) of the histological sections were acquired using the motorized stage of the microscope and the ImageJ stitching tool. The acquired single tiles featured a subsection of 698 μm $\times$ 552 μm with a lateral resolution of 536 nm in both directions. Tiles were acquired with a 7% overlap to enable stitching.

3.4. Visual Inspection

Immediately after exposure to the laser energy, images of the lesion patterns were taken using a digital microscope (Reflecta GmbH, Rottenburg, Germany) with a magnification of 40x. The retinal lesions were classified manually into four classes by two independent observers. The “Strong Visible” (SV) class includes lesions creating a clearly visible spot on the retina and a visible distortion of the layers. This lesion class shows affected tissue within an area larger than the spot size of the treatment laser and tended to further increase in size for 10–30 minutes after laser application. The “Visible” (V) class includes lesions that are still clearly visible but did not show any layer distortion or size increase after laser application. The “Barely Visible” (BV) and the “Invisible” (IV) class include the lesions that were barely visible as grayish spots and the lesions that could not be detected ophthalmoscopically, respectively.

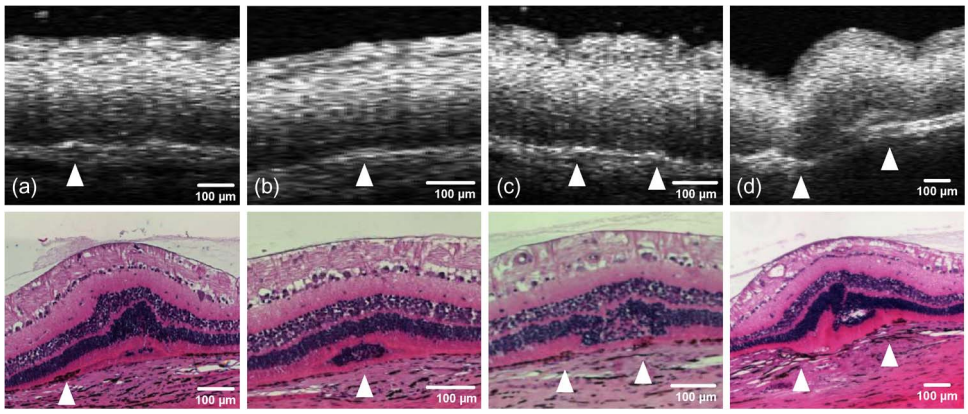

Fig. 2. Comparison of OCT scans and histological sections from corresponding lesions found using retinal landmarks. (a)–(d) Lesions with tissue effects in the lower retinal layers; in (d), upper retinal layers are also affected. Arrows mark corresponding features in both modalities. Retinal bulging as seen in the histological sections is likely a fixation artifact not experienced in the in-situ OCT scans.

4. Experimental Results

In order to evaluate the imaging capabilities of the custom-designed OCT system during laser therapy, OCT scans of lesions were compared to histological sections from the same sample. Ex-vivo porcine eyes were treated and prepared for histology as described in Sections 3.2 and 3.3. The used lesion patterns included laser lesions with varying laser energy as well as high-energy markers. Immediately after the application of the laser energy, one unaveraged 10 mm $\times$ 10 mm OCT volume with 750 $\times$ 750 $\times$ 2048 pixels was acquired and post-processed offline. The eyes were prepared for histology as described before. In order to compare the OCT data with histology, laser lesions were identified in both OCT and histology with the help of landmarks such as high-energy lesions, blood vessels and the optic nerve head.

Fig. 2 shows examples of four corresponding laser lesions in OCT and histology. Lesions in OCT and histology were matched manually using histology tile scans and OCT volume scans based on retinal landmarks as described before. Only lesions that could be matched with certainty were evaluated. Images (a)–(c) represent lesions with tissue effects limited to the lower retinal layers, in image (d) also the upper layers are clearly affected. The reduced OCT image quality and the loss of optical properties in the neural layers is typical for enucleated porcine eyes. The image quality and the representation of retinal layers correspond to other publications using similar protocols [11], [24]. Nevertheless, it can be noted that OCT is capable of detecting small structural changes, especially when affecting the RPE/Bruch's Membrane complex or the IS/OS junction. Thickening, deformation or disruption of the RPE and its surrounding layers give rise to changes in optical properties that can be detected in the OCT scans. The scans seemingly fail to accurately represent folding and thickenings of the outer nuclear and outer plexiform layer. It remains unclear if those foldings were present at the time of OCT imaging or are an artifact as a result of fixation and preparation for histology.

During the application of the laser lesions, time-lapse scans were acquired simultaneously approximately in the center of the lesion by carefully combining and aligning the OCT and treatment laser using the dichroic mirror and the SDO. Mscans were taken with 60 kHz Ascan rate and an integration time of 14 μs. Fig. 3 shows intensity Mscans of approximately 40 ms from lesions that were classified as “Invisible” according to Section 3.4. In both Mscans the tissue effects causing a change in optical signal seem to originate in the RPE/Bruch's complex and are expanding over the full thickness of the neural retina within approximately 2.2 ms–2.3 ms (dotted yellow arrows). After the laser energy deposition, the residual optical changes appear to be limited to the RPE/Bruch's complex which is in close agreement to effects observed by Mueller *et al.* [11] at comparable laser energy.

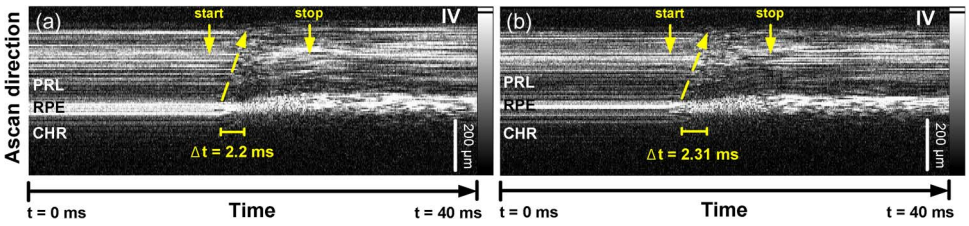

Fig. 3. Intensity Mscans of retinal laser lesions acquired with 60 kHz Ascan rate and 14 μs integration time. (a) and (b) Invisible (IV) lesions from the same sample but different positions. Dotted yellow arrows highlight the outward expansion of the optical effects to upper retinal layers, and solid yellow arrows mark the start and stop of the laser application. Layers are labeled PRL: photoreceptor layer, RPE: retinal pigment epithelium, and CHR: choroid. Neural retinal layers were not labeled in detail as they cannot be distinguished in ex-vivo OCT scans.

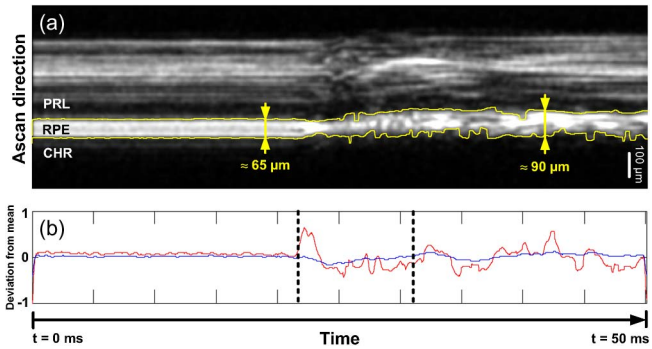

Fig. 4. Intensity Mscans of an invisible retinal laser lesion acquired with 60 kHz Ascan rate and 14 μs integration time. (a) Scan with segmented RPE/Bruch's complex and optical effects in the tissue starting in the RPE. (b) Variation of the average intensity from the mean value of the entire retina (blue line) and the RPE/Bruch's complex only (red line). The dotted vertical black lines mark the start and end of the laser application. Layers are labeled PRL: photoreceptor layer, RPE: retinal pigment epithelium, and CHR: choroid. Neural retinal layers were not labeled in detail as they cannot be distinguished in ex-vivo OCT scans.

Additionally, the RPE/Bruch's complex in the Mscans of the invisible lesion was filtered using an anisotropic filter, segmented and analyzed as shown in Fig. 4(a). Fig. 4(b) shows the variation of the average Mscan pixel intensity from the mean intensity value over time which is linked to changes of the scattering coefficients. Values were calculated for the complete retina including the neural layers and the RPE/Bruch's complex (blue line), as well as for the RPE/Bruch's complex only (red line). Figure (b) shows a higher sensitivity of depth resolved analysis (i.e., RPE/Bruch's only) to changes in scattering during and after laser coagulation compared to the average value for all retinal layers which remains relatively unchanged. The reflective layer complex including RPE and Bruch's membrane expanded from approximately 65 μm to 90 μm (refractive index corrected with $n = 1.38$ [25]).

For the evaluation of the visibility threshold of the laser lesions in visual inspection and with the proposed OCT system, four porcine retina samples were treated with spots with a total irradiation time of 10 ms but varying deposited laser energy. Each lesion was assessed visually in the fundus images directly after laser application. OCT scans were taken immediately after all laser lesions were applied to the sample.

Fig. 5 shows examples of the classes for visual inspection [see Fig. 5(a)–(d)], as described in Section 3.4, as well as examples for the visibility of such lesions in OCT imaging [see Fig. 5(e) and (f)]. For the analysis of the visibility threshold in OCT imaging, lesions were only classified as visible or invisible. Lesions were classified as visible if at the very minimum a small hyperreflectivity in or above the RPE occurred [i.e., Fig. 5, (f)].

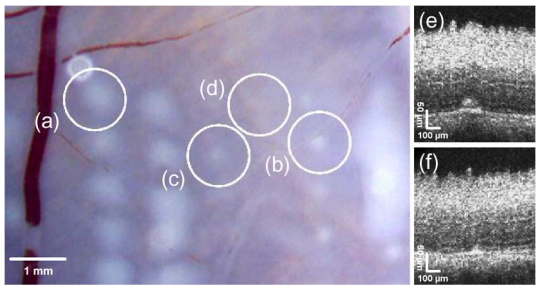

Fig. 5. Classes of visibility in fundus and OCT imaging. Examples are marked for the strongly visible [SV, (a)], visible [V, (b)], barely visible [BV, (c)], and invisible [IV, (d)] classes used for visual inspection, whereas (e) and (f) show examples for lesions visible in OCT imaging with (f) representing the minimal optical changes that were considered as a visible lesion in OCT.

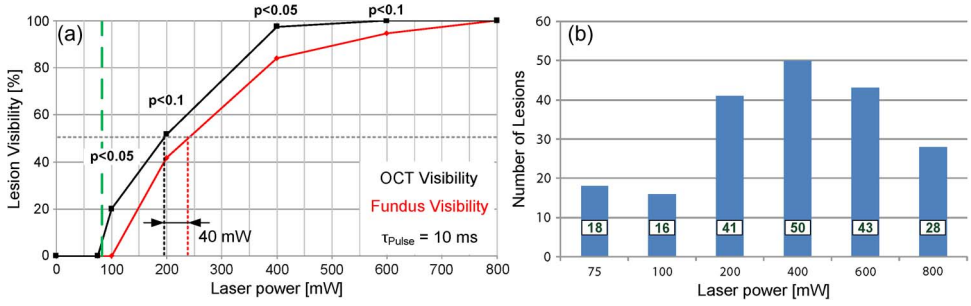

Fig. 6. Visibility of laser lesions depending on laser energy for visual inspection and OCT imaging. The dotted green line represents the recalculated visibility threshold for autofluorescence imaging found by Muqit *et al.* [10]. The 50% visibility threshold energy was calculated to be 195 mW for OCT and 235 mW for visual inspection. In two cases, statistical significance was $p < 0.05$ and $p < 0.1$ otherwise. (b) Distribution of the number of evaluated lesions per energy for results presented in Figs. 6(a) and 7.

Lesions that created a large distortion of the retinal layers and where lower retinal layers could no longer be detected due to shadowing effects were excluded from the statistics. Lesions that could not be found in OCT were classified as invisible if OCT quality at the expected position of the lesion was sufficient.

A total of 196 lesions were classified according to the previously presented classes in visual inspection and as visible or invisible in the corresponding OCT scans. Lesion visibility was defined as the percentage of at least barely visible lesions. Fig. 6(a) presents the lesion visibility depending on the laser energy and the calculated threshold energies for 50% ophthalmoscopic and OCT visibility. The dotted green vertical line represents the visibility threshold for autofluorescence imaging found in rabbits by Muqit *et al.* [10] and recalculated to the laser parameters used in this paper assuming linear laser effects. With OCT, laser lesions were typically detected with a laser power 40–50 mW below the ophthalmoscopic visibility threshold. For 100% visibility, this difference increased 4-fold to a value of 200 mW. Statistical confirmation was executed using the Chi-Square test at all laser energies where visibility was neither 0% nor 100% in both distributions. In two cases, a p-value of $0.05 < p$ was found, in the remaining two cases it was $0.05 < p < 0.1$. Fig. 6(b) shows the distribution of the examined laser lesions by laser energy.

Fig. 7 shows OCT visibility linked to the four previously presented ophthalmoscopic classes as well as the distribution of the number of lesions per laser energy. In this analysis, 42.2% of lesions $(N = 19)$ that were classified as invisible by visual inspection could be detected in OCT scans. Laser spots with laser energy below 50 mW (or 0.5 mJ total deposited energy) and, therefore, below the visibility threshold of both modalities according to Fig. 6 were excluded from the statistics.

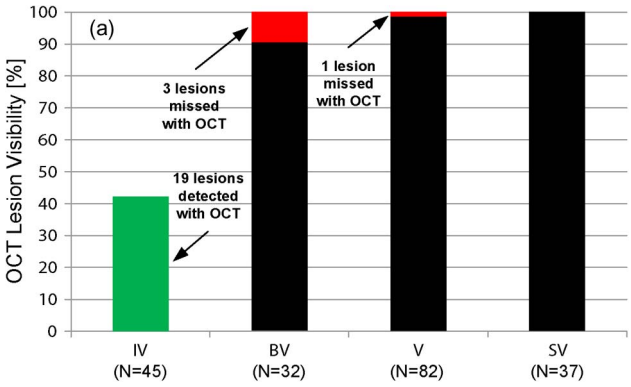

Fig. 7. Percentage of visible lesions in OCT according to the visual classification of lesions. Green bars represent the lesions only detected by OCT, red bars represent the lesions only detected ophthalmoscopically and missed by OCT, and black bars represent lesions detected with both modalities.

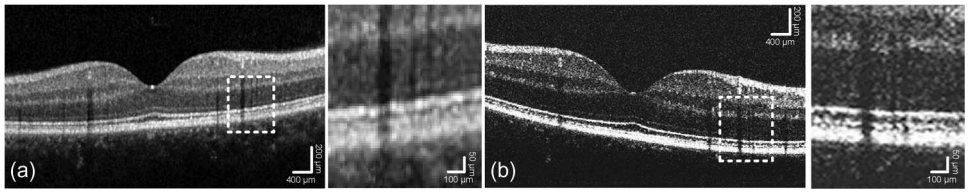

Fig. 8. Scans of the macular region of a healthy male subject taken with the Heidelberg Spectralis (a) and the proprietary OCT system (b). Scans were taken at an approximately identical position with both systems at 40 kHz (Spectralis) and 60 kHz (own system) and matched manually using landmarks. Scans were averaged four times in both systems. Detailed views to the right of each scan show a sub-region of the scan as indicated by the white boxes.

The proposed OCT system was further tested on healthy human subjects and results compared to scans of a clinical system with an axial resolution of approximately 7 μm in air (Heidelberg Spectralis HRA, Heidelberg Engineering, Germany). Fig. 8 shows scans of the retina of a healthy 30-year-old male subject, recorded with the Heidelberg Spectralis (a) and the custom-made OCT system (b). Scans were taken with an integration time of 25 μs (Spectralis) and 14 μs (own system) with approximately the same measurement area, sampling density and incident laser power according to IEC safety standards [26]. Scans were averaged four times in both systems and processing was executed by the Spectralis software and the LabVIEW framework, respectively. For averaging, the Spectralis software used frame-to-frame averaging whereas with the proposed system, Ascans taken consecutively at the same position were averaged which may explain the notable differences in dynamic range between the proposed OCT system and the Spectralis. Initially designed for static setups with no eye movements, the Ascan by Ascan averaging of the proprietary OCT system results in a reduced speckle suppression compared to frame-by-frame averaging when eye movements are present.

In Fig. 8, for each scan a detailed view is presented emphasizing the visibility of the lower retinal layers in both systems. Despite the fact that the clinical system shows a better overall image quality, it is evident, that the three times higher axial resolution of the proposed system reveals additional details of the layers neighbouring the RPE layer, which leads to a more reliable detection of optical changes in these layers in living subjects.

5. Conclusion

In this paper we have shown that OCT images taken with an ultra-high axial resolution system are capable of depicting small changes in reflectivity and layer orientation during and

immediately after the application of the laser energy in retinal photocoagulation. Histological sections showed a variety of artifacts such as retinal swelling and bulging which are not observed in in-vivo experiments or the in-situ OCT scans, but comparison of OCT scans with histological overview stainings showed identical features concerning changes in the IS/OS junction or the RPE layer.

Real-time Mscans showed optically visible tissue effects with changes in reflectivity and thickness starting at the RPE layer and expanding towards the upper retinal layers in ophthalmoscopically invisible cases. The observed effects are comparable to the data found by Mueller *et al.* [11] but showed additional details due to the higher axial resolution of the used system. Segmentation and depth-resolved analysis of the reflective complex at the RPE show a higher sensitivity for changes in mean intensity during and after laser application when compared to the analysis of the overlying neural retinal layers.

OCT imaging lowered the lesion visibility threshold by at least 40 mW compared to ophthalmoscopic inspection and 42% of ophthalmoscopically invisible lesions were detected using OCT. Lesion visibility was higher for OCT imaging at all energies and results were partly confirmed statistically using Chi-Square test with p-values of $0.05 < p$ for measurement points 100 mW and 400 mW and a value of $0.05 < p < 0.1$ for measurement points at 200 mW and 600 mW. The 50% visibility threshold was found to be 195 mW in OCT and 235 mW for ophthalmoscopic inspection with a pulse duration of 10 ms. In their experiments, Muqit *et al.* [10] found OCT visibility thresholds to be less than 50 mW lower than the value for barely visible ophthalmoscopic lesions. Recalculated to the spot size and laser parameters used in this paper, this leads to an equivalent energy difference between OCT and ophthalmoscopic visibility thresholds of just over 5 mW, almost eight times lower than the values found in the presented experiment. Other publications found considerably lower ophthalmoscopic visibility thresholds for coagulation in living subjects such as rabbits (132 μm spot, 10 ms pulse width, 150 mW) [22]. Those values imply that absolute effects of laser-tissue interaction in ex-vivo samples are difficult to compare to in-vivo experiments. Direct comparison is further aggravated by different treatment wavelengths, spot sizes and pulse parameters. However, relative comparison of energy thresholds is considered to be valid and treatment energy could be reduced by 17% in the presented experiments compared to 12% by Muqit *et al.* where the therapeutic window with 20 ms pulses was larger than for 10 ms pulses [22].

OCT scans of enucleated eyes suffer from the drawback of losing a variety of optical properties typical to the retina. Laser effects in the outer nuclear layer and the outer plexiform layer are hard to estimate from the scans recorded with our experimental setup as information from those layers is reduced. Thus, the benefit of an ultra-high axial resolution OCT system appears to be very limited for enucleated porcine eyes. However, when comparing imaging techniques on human subjects the value of the increased axial resolution becomes more evident. We expect the difference between lesion visibility in OCT and ophthalmoscopic inspection to further increase when treating living subjects. With the inclusion of a sophisticated registration scheme and frame-to-frame averaging, the inevitable eye movements of the patients will greatly reduce the signal-degrading speckle, potentially enabling sub-resolution information to be acquired from the scattering structure [16]. In the case of selective retina therapy (SRT) [27]–[29], this effect might become even more important due to the confinement of the lesions to the RPE layer and the larger therapeutic window compared to continuous irradiation [30]. In-vivo examinations of the retina at the level of the RPE and Bruch's Membrane with conventional and selective treatment are the scope of an ongoing study.

To conclude, the found results from volume and simultaneous Mscan imaging support the hypothesis that laser coagulation effects will first be detectable in the RPE/Bruch's complex and with a suitable axial resolution, tissue changes in the RPE layer may be detected earlier and more reliably possibly facilitating a more conclusive detection of retinal laser damage immediately after laser application. We have shown that an OCT system specifically designed for the imaging of the thin retinal layers yields a better visibility of conventional laser lesions and a large number of ophthalmoscopically invisible lesions could be detected directly after irradiation using

the proposed OCT system. With such an online monitoring, time consuming and expensive angiographies as treatment control would eventually become obsolete while a less minimally-invasive laser therapy could enable a preventive treatment of retinal diseases.

Acknowledgement

The authors would like to express their gratitude to F. Bisignani and A. Schweri-Olac of the Histology Laboratory, Ophthalmologic Department, Inselspital, Bern, Switzerland, for their valuable support during the processing and preparation of the histological sections. The support from the Meridian AG for providing the Merilas 577 laser prototype is greatly acknowledged.

References

[1] R. Brinkmann and R. Birngruber, "Selektive Retina-Therapie (SRT)," *Z. Med. Phys.*, vol. 17, no. 1, pp. 6–22, 2007.
[2] S. Koinzer *et al.*, "Comprehensive detection, grading, and growth behavior evaluation of subthreshold and low intensity photocoagulation lesions by optical coherence tomographic and infrared image analysis," *Biomed Res. Int.*, vol. 2014, 2014, Art. ID. 492679.
[3] D. Huang *et al.*, "Optical coherence tomography," *Science*, vol. 254, no. 5035, pp. 1178–1181, Nov. 1991.
[4] L. Reznicek *et al.*, "Megahertz ultra-wide-field swept-source retina optical coherence tomography compared to current existing imaging devices," *Graefes Arch. Clin. Exp. Ophthalmol.*, vol. 252, no. 6, pp. 1009–1016, Jun. 2014.
[5] V. P. Gabel, "Die Lichtabsorption am Augenhintergrund," Habilitation, Muenchen, Germany, Ludwig-Maximilians-Univ. Muenchen, 1974.
[6] V. P. Gabel, R. Birngruber, and F. Hillenkamp, "Visible and near infrared light absorption in pigment epithelium and choroids," in *Proc. 23rd Consilium Ophthalmol.*, Kyoto, Japan, 1978, pp. 658–662.
[7] R. W. Young, "Pathophysiology of age-related macular degeneration," *Surv. Ophthalmol.*, vol. 31, no. 5, pp. 291–306, Mar./Apr. 1998.
[8] M. F. Marmor, "New hypotheses on the pathogenesis and treatment of serous retinal detachment," *Graefes Arch. Clin. Exp. Ophthalmol.*, vol. 226, no. 6, pp. 548–552, 1988.
[9] D. Weinberger, S. Fink-Cohen, D. D. Gaton, E. Priel, and Y. Yassur, "Nonretinovascular leakage in diabetic maculopathy," *Br. J. Ophthalmol.*, vol. 79, no. 8, pp. 728–731, Aug. 1995.
[10] M. M. K. Muqit *et al.*, "Spatial and spectral imaging of retinal laser photocoagulation burns," *Invest. Ophthalmol. Vis. Sci.*, vol. 52, no. 2, pp. 994–1002, Feb. 2011.
[11] H. H. Müller *et al.*, "Imaging thermal expansion and retinal tissue changes during photocoagulation by high speed OCT," *Biomed. Opt. Exp.*, vol. 3, no. 5, pp. 1025–1046, May 2012.
[12] S. Koinzer *et al.*, "Temperature controlled retinal photocoagulation—A step toward automated laser treatment," *Inv. Ophthal. Vis. Sci.*, vol. 53, no. 7, pp. 3605–3614, Jun. 2012.
[13] C. Toth *et al.*, "Correlation between optical coherence tomography, clinical examination and histopathology of macular laser lesions," *Inv. Ophthal. Vis. Sci.*, vol. 36 no.4, pp. 188–198, 1995.
[14] J. Lammer *et al.*, "Imaging retinal pigment epithelial proliferation secondary to PASCAL photocoagulation in vivo by polarization-sensitive optical coherence tomography," *Amer. J. Opthalmol.*, vol. 155, no. 6, pp. 1058–1067, Jun. 2013.
[15] S. Koinzer *et al.*, "Correlation with OCT and histology of photocoagulation lesions in patients and rabbits," *Acta Ophthalmol.*, vol. 91, no. 8, pp. e603–e611, Dec. 2013.
[16] C. Torti *et al.*, "Adaptive optics optical coherence tomography at 120,000 depth scans/s for non-invasive cellular phenotyping of the living human retina," *Opt. Exp.*, vol. 17, no. 22, pp. 19382–19400, Oct. 2009.
[17] M. J. Hogan and J. E. Weddell, *Histology of the Human Eye: An Atlas and Textbook*. Philadelphia, PA, USA: Saunders, 1971.
[18] M. Boulton and P. Dayhaw-Barker, "The role of the retinal pigment epithelium: Topographical variation and ageing changes," *Eye*, vol. 15, no. 3, pp. 384–389, Jun. 2001.
[19] J. K. Luttrull, D. C. Musch, and M. A. Mainster, "Subthreshold diode micropulse photocoagulation for the treatment of clinically significant diabetic macular oedema," *Brit. J. Ophthalmol.*, vol. 89, no. 1, pp. 74–80, Jan. 2005.
[20] T. J. Desmettre, S. R. Mordon, D. M. Buzawa, and M. A. Mainster, "Micropulse and continuous wave diode retinal photocoagulation: Visible and subvisible lesion parameters," *Brit. J. Ophthalmol.*, vol. 90, no. 6, pp. 709–712, Jun. 2006.
[21] Y. M. Paulus *et al.*, "Healing of retinal photocoagulation lesions," *Inv. Ophthalmol. Vis. Sci.*, vol. 49, no. 12, pp. 5540–5545, Dec. 2008.
[22] A. Jain *et al.*, "Effect of pulse duration on size and character of the lesion in retinal photocoagulation," *Arch. Ophthalmol.*, vol. 126, no. 1, pp. 78–85, Jan. 2008.
[23] G. Chidlow, M. Daymon, J. P. M. Wood, and R. J. Casson, "Localization of a wide-ranging panel of antigens in the rat retina by immunohistochemistry: Comparison of Davidson's solution and formalin as fixatives," *J. Histochem. Cytochem.*, vol. 59, no. 10, pp. 884–898, Oct. 2011.
[24] M. Gloesmann *et al.*, "Histologic correlation of pig retina radial stratification with ultrahigh-resolution optical coherence tomography," *Inv. Ophthalmol. Vis. Sci.*, vol. 44, no. 4, pp. 1696–1703, Apr. 2003.
[25] D. Y. Kim *et al.*, "In vivo volumetric imaging of human retinal circulation with phase-variance optical coherence tomography," *Biomed. Opt. Exp.*, vol. 2, no. 6, pp. 1504–1513, Jun. 2011.
[26] *Safety of Laser Products—Part 1: Equipment Classification and Requirements*, CENELEC Eur. Norm 60825-1:2007, 2007, German version, Bruxeles, Belgium.

[27] C. Framme *et al.*, "Structural changes of the retina after conventional laser photocoagulation and Selective Retina Treatment (SRT) in spectral domain OCT," *Curr. Eye Res.*, vol. 34, no. 7, pp. 568–579, Jul. 2009.
[28] F. Mojana *et al.*, "Long-term SD-OCT/SLO imaging of neuroretina and retinal pigment epithelium after subthreshold infrared laser treatment of drusen," *Retina*, vol. 31, no. 2, pp. 235–242, Feb. 2011.
[29] R. Brinkmann, and J. Roider, and R. Birngruber, "Selective Retina Therapy (SRT): A review on methods, techniques, preclinical and first clinical results," *Bull. Soc. Belge Ophtalmol.*, vol. 302, pp. 51–69, 2006.
[30] C. Framme *et al.*, "Threshold determinations for selective retinal pigment epithelium damage with repetitive pulsed microsecond laser systems in rabbits," *Ophthal. Surgery Lasers*, vol. 33, no. 5, pp. 400–409, Sep./Oct. 2002.